Super-strong magnetorheological fluids

2001 J. Phys.: Condens. Matter 13 R979

(http://iopscience.iop.org/0953-8984/13/50/202)

INSTITUTE OF PHYSICS PUBLISHING JOURNAL OF PHYSICS: CONDENSED MATTER

J. Phys.: Condens. Matter **13** (2001) R979–R999 PII: S0953-8984(01)21212-0

TOPICAL REVIEW

Super-strong magnetorheological fluids

R Tao

Department of Physics, Temple University, Philadelphia, PA 19122-6082, USA

Received 23 August 2001, in final form 11 October 2001
Published 30 November 2001
Online at stacks.iop.org/JPhysCM/13/R979

Abstract

Magnetorheological (MR) fluids, which can rapidly be changed from a liquid state to a solid state and *vice versa* by a magnetic field, have the potential to revolutionize several industrial sectors. The key issue is to enhance their yield shear stress. This paper reviews the physical mechanism and microstructure of MR fluids. It finds that the weak points of the MR microstructure under a shear force are at the chains' ends. Hence, a general technique, a compression-assisted-aggregation process, is developed to change the induced MR structure to a structure that consists of robust thick columns with strong ends. The scanning electronic micrographic (SEM) images confirm such a structure change. With this approach, MR fluids become super-strong. The enhanced yield stress of MR fluids reaches 800 kPa at a moderate magnetic field.

1. Introduction

Magnetorheological (MR) fluids, which are changed from a liquid state into a solid state and *vice versa* by a magnetic field, have many industrial applications [1]. A typical MR fluid is a suspension of micrometre-sized magnetic particles in a base liquid, such as silicon oil. Surfactants are usually added to alleviate the settling problem. In the absence of an external magnetic field, no net magnetization exists within the particles and MR fluids have a relatively small viscosity. When a magnetic field is applied, the particles are polarized and align in the field direction to form chains and columns. The induced solid structure produces a respectable yield shear stress, exceeding the requirement for several mechanical applications (40 kPa) set by manufacturing engineers [2]. For example, iron-based MR fluids at 40–50% volume fraction have a yield stress of about 100 kPa under a magnetic field of 1 T [3]. As the magnetic field increases further, the strength of the solidified fluid is further strengthened. This process is reversible. Once the magnetic field is removed, MR fluids return back to their original liquid state. The fluids' response time to a magnetic field is of the order of milliseconds.

MR fluids were first discovered by Rabinow in 1948 [4], following the discovery of electrorheological (ER) fluids [5]. After 50 years' research and development, MR fluids began to have industrial applications. Commercial products, such as shock absorbers, linear dampers and MR polishing machines, are now in production and applied in the automobile industry and

other industrial sectors [1, 6]. Currently, MR fluids are considerably stronger than ER fluids, which have a yield stress at or below 10 kPa. This makes MR fluids very attractive. While MR applications are still at an early stage, their impact on the automobile industry, railroad transportation and bridge construction is already notable.

Since the discovery of MR fluids, there has been some expectation that MR fluids may revolutionize certain industrial sectors. This possibility will become reality only if we can enhance the strength of MR fluids. The current strength of MR fluids, for example, is not sufficient for automobile clutches and manufacturing flexible fixtures. Stronger MR fluids are needed for these applications. In addition, it is especially desirable if these strong MR fluids only require a moderate magnetic field. MR applications need electromagnets inside the MR devices. If the required magnetic field is strong, the electromagnets will be heavy and bulky, making the MR device bulky. The electromagnets are also well known for their delay time since the magnetic coils are a RL circuit. To produce a strong magnetic field, the magnetic coils must have a low dc resistance R and a high inductance L. The stronger the magnetic field is, the longer is the delay time. For a large electromagnet, the delay time L/R can be as long as several seconds. While MR fluids themselves respond to an external field rapidly, the delay time of the electromagnets lengthens the response time of MR devices. Only if the required magnetic field is moderate will the size and delay time of electromagnets not become an issue and MR devices will remain agile.

This, however, is not an easy task. Efforts in searching for new MR materials in the past decades achieved limited results. For example, under a magnetic field of $H = 398$ kA m^{-1} (or $B = 0.5$ T), a new iron–cobalt MR fluid at 25% volume fraction produces a yield shear stress of 80 kPa [3], while a carbonyl iron MR fluid at 25% volume fraction has a yield shear stress of 60 kPa [4]. Recently, Ginder and Davis made a finite element calculation for a single-chain structure of MR fluids [7]. After taking the magnetic saturation of iron (2.1 T) into account, they predicted that an iron-based MR fluid at 50% volume fraction with a single-chain structure had its yield shear stress capped by 200 kPa. From their results, to produce a yield stress of 100 kPa requires a magnetic field around 1 T, quite high indeed. This implies that improving the physical properties of magnetic particles alone is unlikely to bring the strength of MR fluids to a required level.

In this paper, we will report a completely different and novel approach that makes MR fluids super-strong. To improve the microstructure of MR fluids is the key. We do not look for new materials, but employ a rapid compression-assisted-aggregation process to force MR fluids to form a microstructure that is much stronger than the single-chain structure. After doing so, the MR fluids greatly exceed the theoretical strength predicted from the single-chain structure. For example, our experiments with an iron-based MR fluid find that, at a moderate magnetic field of $H = 458$ kA m^{-1} ($B = 0.576$ T), the structure-enhanced yield shear stress exceeds 800 kPa, ten times the value without compression-assisted aggregation. In addition, since it is dealing with the fluid's microstructure, this approach is general and applicable to all kinds of MR fluids.

We will first review the physical mechanism and conventional microstructure of MR fluids in section 2 and discuss the rheological property and weak points of the single-chain structure in section 3. The experimental data to identify the weak points will be in section 4. We will then describe our compression-assisted-aggregation experiment and rheological properties of super-strong MR fluids in section 5. The new MR microstructure of these fluids after the compression process (evidence of the improved microstructure) is in section 6. Finally, we will give a phenomenological formula in section 7 and discuss related issues in section 8.

2. Microstructure of MR fluids

When there is no additional force, the conventional microstructure formation in MR fluids is determined by the field-induced polarization, i.e. the same as in ER fluids [8]. Thus, MR and ER fluids should have the same microstructure. Experiments also confirm this conclusion [9, 10].

Let us consider a model of MR fluids consisting of N identical spherical magnetic particles of magnetic susceptibility μ_p in a base liquid of susceptibility μ_f and $\mu_p > \mu_f = 1$. The fluid is placed between two magnetic poles, which are denoted as two planes $z = 0$ and d. The particles have radius a. The applied magnetic field is $\vec{H}_0$ along the z direction. We assume that H_0 is below the particles' magnetic saturation. Then, in the field, the magnetic particles are polarized, obtaining an induced magnetic dipole moment, $\vec{m} = \vec{H}_{\rm loc} a^3(\mu_p - \mu_f)/(\mu_p + 2\mu_f)$, where $\vec{H}_{\rm loc}$ is the local field. Two magnetic dipoles at $\vec{r}_i$ and $\vec{r}_j$ have an interaction

$$U(\vec{r}_{ij}) = m^2\mu_f(1 - 3\cos^2\theta_{ij})/r_{ij}^3 \tag{1}$$

where $r_{ij} = |\vec{r}_{ij}| = |\vec{r}_i - \vec{r}_j|$ and $0 \leqslant \theta_{ij} \leqslant \pi/2$ is the angle between the z direction and the joint line of the two dipoles. The dipolar force acting on the particle at $\vec{r}_i$ by the particle at $\vec{r}_j$ is given by

$$\vec{f}_{ij} = (3m^2\mu_f/r_{ij}^4)[\vec{e}_r(1 - 3\cos^2\theta_{ij}) - \vec{e}_\theta \sin(2\theta_{ij})] \tag{2}$$

where $\vec{e}_r$ is a unit vector parallel to $\vec{r}_{ij}$ and $\vec{e}_\theta$ is a unit vector parallel to $\vec{e}_r \times (\vec{e}_r \times \vec{H}_0)$. The motion of the ith particle is described by a Langevin equation:

$$M\,\mathrm{d}^2\vec{r}_i/\mathrm{d}t^2 = \vec{F}_i - 6\pi a\eta\,\mathrm{d}\vec{r}_i/\mathrm{d}t + \vec{R}_i(t) \tag{3}$$

where $\vec{F}_i$ is the electric force on the ith dipole from all the other dipoles and all images, η is the viscosity of the base liquid, $-6\pi a\eta\vec{v}_i$ is the Stokes' drag force, the leading hydrodynamic force on the particle, $\vec{R}_i(t)$ is the random Brownian force and M is the particle's mass. Under the dipolar approximation, it is easy to derive analytic expressions for $\vec{F}_i$ from equation (2) [11]. The Brownian force has a white-noise distribution: the averages $\langle R_{i,\alpha}\rangle = 0$ and $\langle R_{i,\alpha}(0)R_{i\beta}(t)\rangle = 12\pi a k_{\rm B}T\eta\delta_{\alpha\beta}\delta(t)$, where $k_{\rm B}$ is the Boltzmann constant and T is the temperature.

The molecular dynamics simulation of the Langevin equation (3) provides a clear picture of the dynamic structure formation of MR fluids. As shown in figure 1, the particles are randomly distributed before a magnetic field is applied. At this stage, the MR fluid is a suspension. At $t = 0$ a magnetic field is turned on and the particles begin to move according to equation (3). As shown in figure 2, after 10 ms single chains are formed. While at this stage these chains are not straight and the microstructure has almost no lateral ordering yet, the fluid already has a yield shear stress and its effective viscosity is significantly increased. With time, the microstructure develops into a three-dimensional (3D) ordering structure. As shown in figure 3, at $t = 0.5$ s, the chains are straighter, some chains aggregate together, and a lateral order begins to build up. After 2.2 s, chains move to form thick columns. While the column has a limited thickness in the x–y direction and maintains the field direction as its preferred direction, it is clear from figure 4 that this structure is a crystalline structure. In fact, the columns have a body-centred tetragonal (bct) lattice structure (figure 5) [8].

The above simulation confirms the experimental finding that the formation of a conventional MR microstructure has two developmental stages. The first stage is the chain-formation process, which only takes several milliseconds to complete after the magnetic field is applied. The second stage is a relatively slow process, involving the aggregation of chains into thick columns. In the simulation this process takes several seconds. When the MR system is large, as in the experiment, this process may take a couple of minutes.

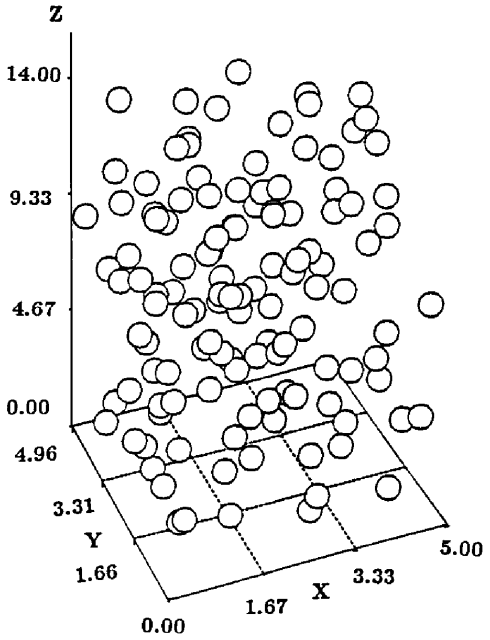

Figure 1. Before a magnetic field is applied, the magnetic particles are randomly distributed in the base liquid.

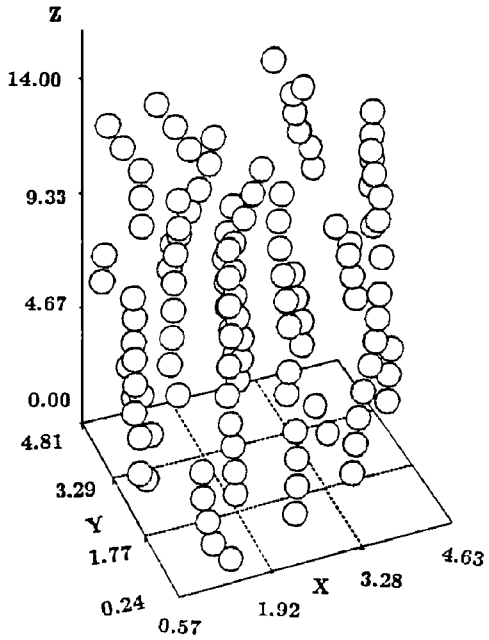

Figure 2. The magnetic particles form chains in about 10 ms after a magnetic field is applied.

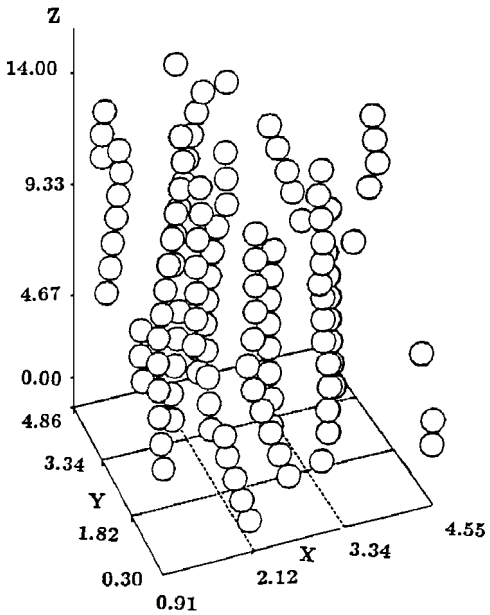

Figure 3. The chains become straighter and some chains aggregate together about 0.5 s after the magnetic field is applied.

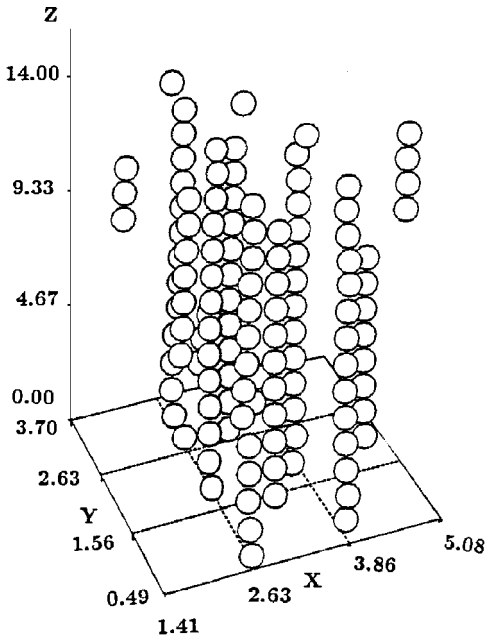

Figure 4. The chains aggregate together to form thick columns, which have a body-centred tetragonal lattice structure.

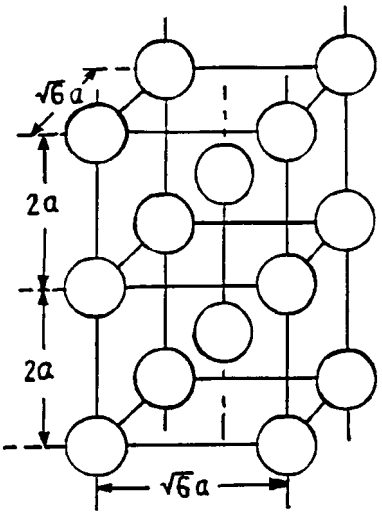

Figure 5. The ground state of the MR structure, body-centred tetragonal lattice. The particles have radius a and are not shown to scale.

The above MR microstructure and the dynamic process can be understood from the induced dipolar interactions. It is clear from equation (1) that the interaction energy is minimized if $\theta_{ij} = 0$ and $r_{ij} = 2a$. Therefore, once we apply a magnetic field, the particles quickly form chains. A finite chain between the two poles, combining with their infinite images, becomes an infinite chain. For the formation of a 3D structure, we need to examine the chain–chain interaction. Let us consider one infinite chain along the z axis with its particles at $z = (2j+1)a$ ($j = 0, \pm1, \pm2, \ldots$). If the second infinite chain parallel to the z axis is a distance ρ away from the first one and its particles are at $z = (2j+1)a + \zeta$, the leading term of the interaction between these two infinite chains is given by

$$U_{cc}(\rho, \zeta) = (m^2 \mu_f \pi^2 / a^3)(2\rho/a)^{1/2} \exp(-\pi\rho/a) \cos(\pi\zeta/a). \tag{4}$$

When $\zeta = 0$, the interaction is repulsive. When $\zeta = a$, all particles in the second chain slide a distance a along the z direction. The two chains become mismatched. Then the interaction energy becomes negative and minimized. The force between such two mismatched chains is attractive. At the final 3D structure, to minimize the energy, every chain must have four mismatched chains as its nearest neighbours. This leads to the bct lattice structure.

In comparison with the dipolar interaction, the Brownian force is very weak. For most MR fluids, the ratio of the interaction energy of two magnetic dipoles to the thermal energy, $\alpha = m^2/(8a^3 k_B T)$, is quite large, $\alpha > 100$. Therefore, at the first stage of chain formation, the Brownian force is negligible in comparison with the interaction between two dipoles. However, once the chains are formed, the dipolar interaction is screened. As noted from equation (4), the interaction between two straight chains is weak and short-ranged. Then the Brownian force plays an important role. For example, if $\alpha = 100$, when the distance between the two straight chains $\rho \sim 3a$, the Brownian force is already compatible with the chain–chain interaction. Then, the Brownian force easily makes the chains bent or randomly fluctuating, as seen in the simulation (figures 2 and 3). This phenomenon is associated with the instability of a one-dimensional solid. The attracting force between curved chains is stronger than that of straight chains [12]. Therefore, the chains' fluctuations under Brownian motion help their aggregation together. However, once several chains get together to form a column, the 3D column is not easy to bend or fluctuate (figure 4). The Brownian force has little effect on columns. Thus the column–column aggregation is difficult in the unassisted aggregation process and the developed columns are of limited thickness.

The rheological properties and strength of MR fluids are related to the field-induced microstructure. For example, a thick column structure is stronger than a single-chain structure [13]. However, most agile MR applications require quick response and cannot wait long enough for the columns to form. Moreover, the unassisted aggregation process only produces columns consisting of 10–15 chains [9]. The relevant MR microstructure in most MR applications is the single-chain structure [7].

3. The weak points of MR microstructure

To develop strong MR fluids, we need to know the rheological properties of the induced MR structures. In particular we want to identify the weak points of these structures and find a way to strengthen them. To begin with, we examine the single-chain structure, which is the basis of all other MR structures.

We consider applying an external shear force on the chain. Under the force, the chain deforms, becomes slanted, then breaks into two broken chains if the shear force exceeds a threshold. The breaking point should be the chain's weak point under the shear. The conventional wisdom assumes that the breaking point is in the middle of a chain [12, 13]. Why is it at the middle? The system is symmetric around the middle between the two poles; based on this symmetry, it is natural to guess that the chain could break at the middle.

However, this is not the case. There is a symmetry breaking [14]. After a magnetic field is applied, the space is no longer isotropic. To form a long chain along the field direction is energetically favoured in this space. Let us assume that the shear process is quasi-static such that the chain relaxes into the lowest energy state at each shearing step. Under such a deformation, the configuration with the minimum energy is no longer symmetric. The symmetric configuration becomes unstable. In particular, during the initial deformation, a gap emerges at one end. The gap widens as the strain increases. When the strain exceeds a critical value, the chain breaks. The breaking point is at either end, but not in the middle. In another words, the weak points of a MR chain under shear are at its two ends.

In order to demonstrate the above points, we apply the Green function method to find the energy for various configurations. The calculation includes the multipole contributions and the effect of electrodes. A comparison of the energies between different configurations enables us to identify the minimum-energy configuration. We thus find the deformation process and locate the breaking point.

After the fluid is activated, chains are formed. The induced attractive force among the chain particles provides a capacity to resist an external stress. The yield shear stress of a chain is defined as the stress, below which a deformed chain can recover after the stress is removed, but above which the chain incurs non-recoverable damage even if the stress is released. It is clear that quantitative estimation of the yield stress depends on how the chain deforms in response to an external stress.

The chain is originally along the field direction, spanning between the electrodes with particles touching each other. Upon application of a pair of shear forces at the chain's two end particles, the chain is strained and elongated. These two forces are of the same magnitude but in the opposite direction, perpendicular to the field. As mentioned before, the shear process is slow and can be described as quasi-static.

Since the magnetic field satisfies $\nabla \times \vec{H} = 0$, we define a magnetic potential $\Phi(\vec{r})$, $\vec{H} = -\nabla\Phi(\vec{r})$. Then $\nabla^2\Phi(\vec{r}) = 0$ with its boundary conditions as $\Phi(\vec{r})|_{z=0} = 0$ and $\Phi(\vec{r})|_{z=d} = -H_0 d$. Here $\vec{H}_0 = H_0\hat{z}$ is the applied magnetic field. We denote $\hat{z}$ as a unit vector along the z direction. On the particle surface, $\Phi_{\text{out}}(\vec{r})|_{s_i} = \Phi_{\text{in}}(\vec{r})|_{s_i}$ and

$\mu_f \frac{\partial \Phi_{\rm out}(\vec{r})}{\partial n_i}\big|_{S_i} = \mu_p \frac{\partial \Phi_{\rm in}(\vec{r})}{\partial n_i}\big|_{S_i}$ where $\Phi_{\rm out}(\vec{r})$ and $\Phi_{\rm in}(\vec{r})$ are the potentials outside and inside the ith particle, respectively. S_i is the ith particle's surface and $\partial/\partial n_i$ is the normal derivative at the surface S_i in the outward direction.

The above boundary problem can be simplified by writing the total potential $\Phi(\vec{r})$ of the system in two terms

$$\Phi(\vec{r}) = -\vec{H}_0 \cdot \vec{r} + \Phi^{(1)}(\vec{r}) \tag{5}$$

where the second term in equation (5) is the magnetic potential due to the polarization of particles by the applied field. The Laplace equation for $\Phi^{(1)}$ and its boundary condition are given by

$$\nabla^2 \Phi^{(1)}(\vec{r}) = 0, \qquad \Phi^{(1)}(\vec{r})|_{z=0} = \Phi^{(1)}(\vec{r})|_{z=d} = 0. \tag{6}$$

The Green function, which equals the potential at $\vec{r}$ due to a unit point magnetic 'charge' at $\vec{r}\,'$ and all its images, is given by

$$G(\vec{r}, \vec{r}\,') = \sum_{k\lambda} \frac{\lambda}{|\vec{r} - \vec{r}\,'_{k\lambda}|} \tag{7}$$

where $k = 0, \pm 1, \pm 2, \ldots, \lambda = \pm 1$, $\vec{r} = (x, y, z)$ and $\vec{r}\,'_{k\lambda} = (x', y', 2kd + \lambda z')$. Application of the Green function yields

$$\Phi^{(1)}(\vec{r}) = \int_V \rho(\vec{r}\,') G(\vec{r}, \vec{r}\,')\, {\rm d}^3 r' \tag{8}$$

where $\rho(\vec{r}\,')$ is the magnetic 'charge' at $\vec{r}\,'$. Since the magnetic 'charge' only appears on the surfaces of particles inside the volume V, equation (8) becomes

$$\Phi^{(1)}(\vec{r}) = \sum_i \oint_{S_i} \sigma(\vec{r}\,') G(\vec{r}, \vec{r}\,')\, {\rm d}a' = \sum_{ik\lambda} \oint_{S_i} \frac{\lambda \sigma(\vec{r}\,')}{|\vec{r} - \vec{r}\,'_{k\lambda}|}\, {\rm d}a' \tag{9}$$

where $\sigma(\vec{r}\,')$ is the surface charge density to be determined by the boundary conditions.

To apply the boundary conditions, we need to express $\Phi(\vec{r})$ in the coordinate system which has its origin at a particle's centre. We therefore make an expansion:

$$\frac{1}{|(\vec{r} - \vec{r}_j) - (\vec{r}\,'_{k\lambda} - \vec{r}_j)|} = 4\pi \sum_{lm} \frac{1}{2l+1} \frac{r_<^l}{r_>^{l+1}} Y^*_{lm}(\vec{r}\,'_{k\lambda} - \vec{r}_j) Y_{lm}(\vec{r} - \vec{r}_j) \tag{10}$$

where $\vec{r}_j$ is the jth particle's centre and $r_<$ (or $r_>$) is the smaller (or larger) one among $|\vec{r} - \vec{r}_j|$ and $|\vec{r}\,'_{k\lambda} - \vec{r}_j|$. For $m \geqslant 0$, the spherical harmonic function $Y_{lm}(\vec{r}) = \sqrt{(2l+1)(l-m)!/[4\pi(l+m)!]} P_l^m(\cos\theta) {\rm e}^{{\rm i}m\phi}$, where P_l^m is an associated Legendre function and θ and ϕ are the spherical coordinates of $\vec{r}$. If $m < 0$, $Y_{lm} = (-1)^m Y_{l\,|m|}$. With the above expansion, we obtain

$$\Phi(\vec{r}) = -H_0 z + 4\pi \sum_{ik\lambda lm} \frac{\lambda}{2l+1} Y_{lm}(\vec{r} - \vec{r}_j) \oint_{S_i} \frac{r_<^l}{r_>^{l+1}} \sigma(\vec{r}\,') Y^*_{lm}(\vec{r}\,'_{k\lambda} - \vec{r}_j)\, {\rm d}a'. \tag{11}$$

In particular, the potentials inside and outside the jth particle are given by

$$\Phi_{\rm in}(\vec{r}) = -H_0 z_j - H_0(z - z_j) + 4\pi \sum_{lm} \frac{q_{jlm}}{(2l+1)a^{2l+1}} |\vec{r} - \vec{r}_j|^l Y_{lm}(\vec{r} - \vec{r}_j)$$
$$+4\pi \sum_{ik\lambda lm}{}' \frac{\lambda}{2l+1} |\vec{r} - \vec{r}_j|^l Y_{lm}(\vec{r} - \vec{r}_j) \oint_{S_i} \frac{\sigma(\vec{r}\,')}{|\vec{r}\,'_{k\lambda} - \vec{r}_j|^{l+1}} Y^*_{lm}(\vec{r}\,'_{k\lambda} - \vec{r}_j)\, {\rm d}a' \tag{12}$$

$$\Phi_{\rm out}(\vec{r}) = -H_0 z_j - H_0(z - z_j) + 4\pi \sum_{lm} \frac{q_{jlm}}{(2l+1)|\vec{r} - \vec{r}_j|^{l+1}} Y_{lm}(\vec{r} - \vec{r}_j)$$
$$+4\pi \sum_{ik\lambda lm}{}' \frac{\lambda}{2l+1} |\vec{r} - \vec{r}_j|^l Y_{lm}(\vec{r} - \vec{r}_j) \oint_{S_i} \frac{\sigma(\vec{r}\,')}{|\vec{r}\,'_{k\lambda}} - \vec{r}_j|^{l+1} Y^*_{lm}(\vec{r}\,'_{k\lambda} - \vec{r}_j)\, {\rm d}a'$$
$$a < |\vec{r} - \vec{r}_j| < |\vec{r}\,'_{k\lambda} - \vec{r}_j| \tag{13}$$

where

$$q_{jlm} = \oint_{S_j} \sigma(\vec{r}\,')a^l Y^*_{lm}(\vec{r}\,' - \vec{r}_j)\,\mathrm{d}a' \tag{14}$$

is the magnetic multipole moment of the jth particle with respect to its centre. The prime on those summation symbols in equations (12) and (13) indicates that the cases with $i = j, k = 0, \lambda = +1$ are excluded in the summations. This notation will be used hereafter throughout the paper.

To evaluate the above integrals, we introduce the following identity [15]:

$$\frac{Y_{lm}(\vec{r}'_{k\lambda} - \vec{r}_j)}{(2l+1)|\vec{r}'_{k\lambda} - \vec{r}_j|^{l+1}} = \sum_{l'm'} A^{lm}_{l'm'}(\vec{r}_j - \vec{r}_{ik\lambda})|\vec{r}'_{k\lambda} - \vec{r}_{ik\lambda}|^{l'} Y_{l'm'}(\vec{r}'_{k\lambda} - \vec{r}_{ik\lambda}) \tag{15}$$

where $\vec{r}_{ik\lambda} = (x_i, y_i, 2kd + \lambda z_i)$, and the expansion coefficient $A^{lm}_{l'm'}(\vec{r}_j - \vec{r}_{ik\lambda})$ is given by

$$A^{lm}_{l'm'}(\vec{r}_j - \vec{r}_{ik\lambda}) = (-1)^{l+m}\frac{Y^*_{l+l',m'-m}(\vec{r}_j - \vec{r}_{ik\lambda})}{|\vec{r}_j - \vec{r}_{ik\lambda}|^{l+l'+1}} \times \left[\frac{4\pi(l+l'+m-m')!(l+l'+m'-m)!}{(2l+1)(2l'+1)(2l+2l'+1)(l+m)!(l-m)!(l'+m')!(l'-m')!}\right]^{1/2}. \tag{16}$$

Substituting equation (15) into equation (12), we have

$$\Phi_{\mathrm{in}}(\vec{r}) = -\vec{H}_0\cdot\vec{r}_j - \vec{H}_0\cdot(\vec{r} - \vec{r}_j) + 4\pi\sum_{lm}\frac{q_{jlm}}{(2l+1)a^{2l+1}}|\vec{r} - \vec{r}_j|^l Y_{lm}(\vec{r} - \vec{r}_j) + 4\pi\sum_{ik\lambda lm}{}' \lambda|\vec{r} - \vec{r}_j|^l Y_{lm}(\vec{r} - \vec{r}_j)\sum_{l'm'} A^{jlm}_{il'm'} \times \oint_{S_i}\sigma(\vec{r}\,p)|\vec{r}'_{k\lambda} - \vec{r}_{ik\lambda}|^{l'} Y^*_{l'm'}(\vec{r}'_{k\lambda} - \vec{r}_{ik\lambda}). \tag{17}$$

For the sake of simplicity, we abbreviate $A^{lm}_{l'm'}(\vec{r}_j - \vec{r}_{ik\lambda})$ as $A^{jlm}_{il'm'}$. Note that, in the above equation, $|\vec{r}'_{k\lambda} - \vec{r}_{ik\lambda}| = a$ and $Y^*_{l'm'}(\vec{r}'_{k\lambda} - \vec{r}_{ik\lambda}) = \lambda^{l'+m'}Y^*_{l'm'}(\vec{r}\,' - \vec{r}_i)$. Equation (17) thus becomes

$$\Phi_{\mathrm{in}}(\vec{r}) = -\vec{H}_0\cdot\vec{r}_j - \vec{H}_0\cdot(\vec{r} - \vec{r}_j) + 4\pi\sum_{lm}\frac{q_{jlm}}{(2l+1)a^{2l+1}}|\vec{r} - \vec{r}_j|^l Y_{lm}(\vec{r} - \vec{r}_j) + 4\pi\sum_{il'm'} q_{il'm'}\sum_{lm} B^{jlm}_{il'm'}|\vec{r} - \vec{r}_j|^l Y_{lm}(\vec{r} - \vec{r}_j) \tag{18}$$

where

$$B^{jlm}_{il'm'} = \sum_{k\lambda}{}' \lambda^{l'+m'+1} A^{lm}_{l'm'}(\vec{r}_j - \vec{r}_{ik\lambda}). \tag{19}$$

Similarly, the potential outside the jth particle is shown to be

$$\Phi_{\mathrm{out}}(\vec{r}) = -\vec{H}_0\cdot\vec{r}_j - \vec{H}_0\cdot(\vec{r} - \vec{r}_j) + 4\pi\sum_{lm}\frac{q_{jlm}}{(2l+1)|\vec{r} - \vec{r}_j|^{l+1}}Y_{lm}(\vec{r} - \vec{r}_j) + 4\pi\sum_{il'm'} q_{il'm'}\sum_{lm} B^{jlm}_{il'm'}|\vec{r} - \vec{r}_j|^l Y_{lm}(\vec{r} - \vec{r}_j). \tag{20}$$

From the boundary condition on the sphere surfaces, we have

$$(\mu_p - \mu_f)\left\{\frac{H_0}{\sqrt{12\pi}}Y_{10}(\vec{r} - \vec{r}_j) - \sum_{lm} l a^{l-1}\left[\sum_{il'm'} B^{jlm}_{il'm'} q_{il'm'}\right]Y_{lm}(\vec{r} - \vec{r}_j)\right\} = \sum_{lm} q_{jlm}\frac{l\mu_p + (l+1)\mu_f}{(2l+1)a^{l+2}}Y_{lm}(\vec{r} - \vec{r}_j). \tag{21}$$

Applying the orthonormal condition of the spherical harmonics, we find the following relationship among the multipole moments:

$$\sum_{il'm'}\left[\delta_i^j\delta_{l'}^l\delta_{m'}^m+(2l+1)\frac{(\mu_p-\mu_f)a^{2l+1}l}{l\mu_p+(l+1)\mu_f}B_{l'm'}^{lm}\right]q_{il'm'}=\sqrt{\frac{3}{4\pi}}\frac{(\mu_p-\mu_f)a^3}{\mu_p+2\mu_f}H_0\delta_l^1\delta_m^0 \tag{22}$$

or in matrix notation

$$Cq=b \tag{23}$$

where

$$C_{il'm'}^{jlm}=\delta_i^j\delta_{l'}^l\delta_{m'}^m+(2l+1)\frac{(\mu_p-\mu_f)a^{2l+1}l}{l\mu_p+(l+1)\mu_f}B_{il'm'}^{jlm} \tag{24}$$

q represents the multipole moments and b is the matrix given by

$$b_{ilm}=\sqrt{\frac{3}{4\pi}}\frac{(\mu_p-\mu_f)a^3}{\mu_p+2\mu_f}H_0\delta_l^1\delta_m^0. \tag{25}$$

Now let us calculate the interaction energy due to the presence of magnetic particles, ΔW. After assuming that μ_f and μ_p are constants, we have

$$\Delta W=\frac{1}{8\pi}\int(\boldsymbol{H}\cdot\boldsymbol{B}-\boldsymbol{H_0}\cdot\boldsymbol{B_0})\,\mathrm{d}^3x \tag{26}$$

where $\vec{H}$ and $\vec{B}$ ($\vec{H}_0$ and $\vec{B}_0$) are the magnetic field and the flux density after (before) the presence of the particles. Equation (26) is transformed into

$$\Delta W=\frac{1}{8\pi}\int(\vec{H}\cdot\vec{B}_0-\vec{H}_0\cdot\vec{B})\,\mathrm{d}^3x+\frac{1}{8\pi}\int(\vec{H}+\vec{H}_0)\cdot(\vec{B}-\vec{B}_0)\,\mathrm{d}^3x. \tag{27}$$

It is easy to verify that the second integral in equation (27) vanishes. Consequently, ΔW becomes

$$\Delta W=\frac{1}{8\pi}\int(\vec{H}\cdot\vec{B}_0-\vec{H}_0\cdot\vec{B})\,\mathrm{d}^3x. \tag{28}$$

The above integral is taken over the whole region of the system. Only those regions occupied by the particles contribute to the integral since the integrand vanishes outside the particles: as $\vec{B}=\mu_f\vec{H}$ and $\vec{B}_0=\mu_f\vec{H}_0$ outside the particles, $\vec{H}_0\cdot\vec{B}-\vec{H}\cdot\vec{B}_0=0$. Then equation (28) becomes

$$\Delta W=-\frac{(\mu_p-\mu_f)}{8\pi}\sum_{i=1}^{N}\int_{V_i}\vec{H}_0\cdot\vec{H}\,\mathrm{d}^3x \tag{29}$$

where V_i is the volume of the ith particle. Since $\vec{H}_0=-\nabla\Phi_0$ and $\Phi_0=-H_0r\cos\theta$, we have

$$\int_{V_i}\vec{H}_0\cdot\vec{H}\,\mathrm{d}^3x=-\int_{V_i}(\nabla\Phi_0)\cdot\vec{H}\,\mathrm{d}^3x=-\int_{V_i}\nabla\cdot(\Phi_0\vec{H})\,\mathrm{d}^3x+\int_{V_i}\Phi_0\nabla\cdot\vec{H}\,\mathrm{d}^3x. \tag{30}$$

The second integral vanishes because $\nabla\cdot\vec{H}=0$ inside the particle. Applying the divergence theorem to the first integral, we find

$$\int_{V_i}\vec{H}_0\cdot\vec{H}\,\mathrm{d}^3x=-\oint_{S_i}\Phi_0H_n\,\mathrm{d}a \tag{31}$$

where H_n is the normal component of the magnetic field on the inside surface of the particle. Note that $\mu_pH_n^{\mathrm{in}}|_{S_i}=\mu_fH_n^{\mathrm{out}}|_{S_i}$ and the surface 'charge' density $\sigma(\vec{r})$ on the ith particle is

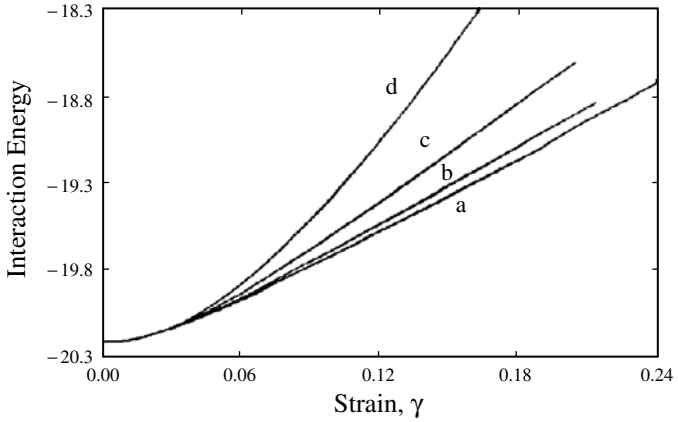

Figure 6. A comparison of the interaction energies for different slanted chains: (a) only one gap between the first and second particles, (b) only one gap at the chain middle, (c) two gaps with one between the first and second particles and the other between the last and next to last particles, and (d) gaps uniformly distributed along the chain.

given by $\sigma(\vec{r}) = (H_n^{\text{out}}|_{S_i} - H_n^{\text{in}}|_{S_i})/4\pi$. Hence, $H_n^{\text{in}}|_{S_i} = 4\pi\sigma(\vec{r})\mu_f/(\mu_p - \mu_f)$. Substituting $H_n^{\text{in}}|_{S_i}$ into equation (31), we have

$$\int_{V_i} \vec{H}_0 \cdot \vec{H}\, \mathrm{d}^3x = \frac{4\pi H_0 \mu_f}{\mu_p - \mu_f} \int_{S_i} \sigma(\vec{r}) r \cos\theta \, \mathrm{d}a = \frac{4\pi H_0 \mu_f}{\mu_p - \mu_f} \sqrt{\frac{4\pi}{3}} q_{i10}. \tag{32}$$

The energy is given in the following form:

$$\Delta W = -\frac{1}{2}\sqrt{\frac{4\pi}{3}} H_0 \sum_{i=1}^{N} q_{i10} \tag{33}$$

where we use $\mu_f = 1$.

The procedure for calculation is as follows. We first calculate matrix C from equation (24) for various configurations, then solve q from equation (23). Afterwards, we calculate the energy from equation (33) for these configurations.

The energy calculation converges quickly as more multipole moments are included. When a pair of shear forces is applied to a chain through the pole plates, as in most MR applications, we assume that the pair of shear forces is applied to the first particle and the last particle in the chain. It is clear that, when the sheared chain is slanted, it is also stretched. In order to locate the breaking point, we first examine where the gap or gaps should be due to this stretch. With various proposed configurations, we calculate the energies for all them and, afterwards, make a comparison. Figure 6 shows the energies for several of these configurations: (1) gaps uniformly distributed along the chain, (2) two gaps, one between the first and second particles and the other between the last and next to last particles, (3) only one gap between the first and second particles, and (4) only one gap in the middle of the chain. It is clear from figure 6 that, when the chain has just one gap between the first and second particles, the energy is the lowest. The configuration with one gap in the middle or the configuration, with gaps uniformly distributed along the chain, never has the lowest energy. This means that, under the external shear force, the slanted chain first has one gap between the first and second particles. Obviously, this gap will get wider and wider if the shear strain become larger and larger.

When the shear strain is big enough, the chain breaks. Where is the breaking point? In figure 7, we plot the energy for the broken chains with several different possible broken points.

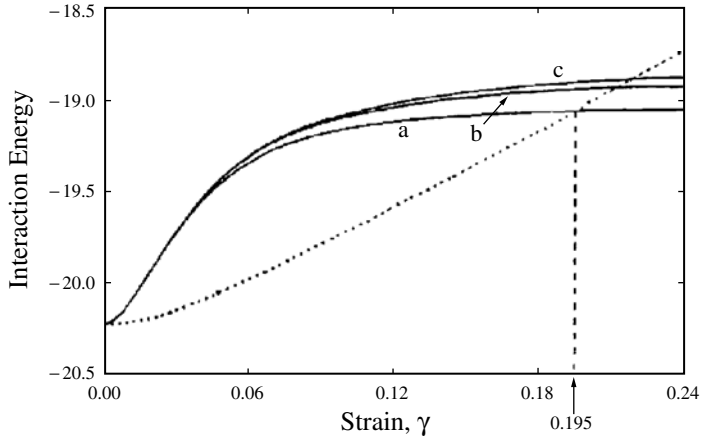

Figure 7. A comparison of the interaction energies for different broken chains: (a) the breaking point is between the first and second particles; (b) the breaking point is between the second and third particles; (c) the breaking point is in the middle. The dotted curve is for a slanted chain with a gap between the first and second particles.

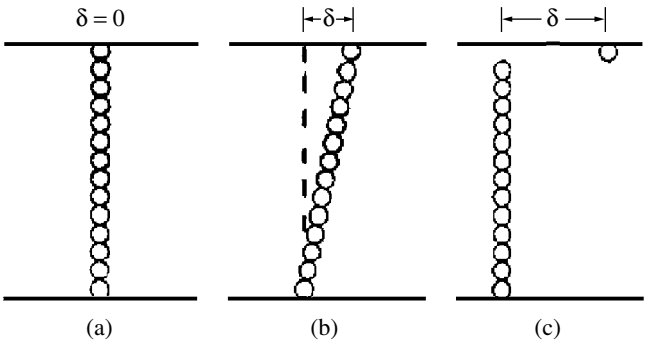

Figure 8. (a) A single chain without shear. (b) A slanted chain under a small shear strain. The gap is between the first and second particles. (c) A broken chain when the shear strain exceeds the critical value.

When the broken point is between the first and second particles, the energy is the lowest among them. The broken chain with the broken point in the middle does not have the lowest energy. Therefore, when the chain breaks under the shear, the broken point must be at one of its ends. This implies that the weak points of a MR chain are at its two ends.

The above theoretical result is outlined in figure 8. When the shear strain is small, the chain becomes slanted and the gap between the first particle and second particle increases. When the shear strain exceeds a critical value, the chain breaks at one of its ends and the broken chain returns to the vertical position.

The critical shear strain for the chain to break is just the cross point between the curve for the slanted chain and the curve for the broken chain (figure 7). From our calculation, this critical shear strain is 0.195.

As mentioned early, the above discussion assumes that the shear process is slow enough that the chain relaxes into the minimum energy state at each shearing step. Since most MR fluids have a response time of the order of milliseconds, we expect that this assumption could

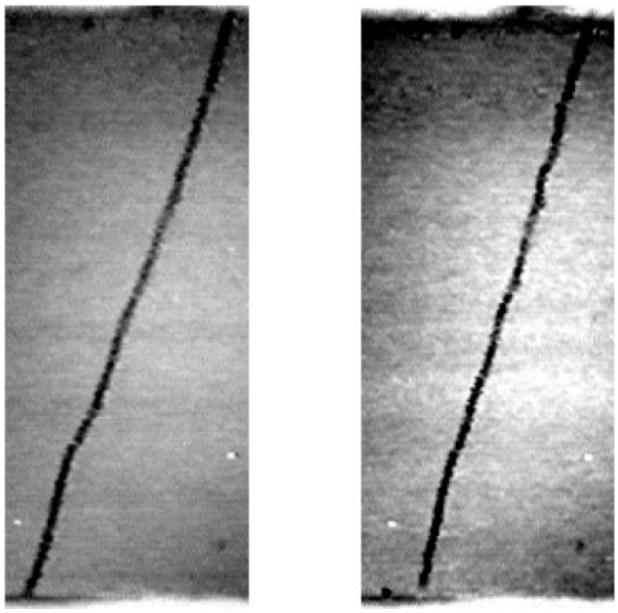

(a) (b)

Figure 9. (a) Under a shear force, the ER chain becomes slanted. (b) The chain breaks between the first and second particles when the shear strain exceeds the critical value.

hold if the shear rate γ is not too high, such as below 100 s^{-1}. Of course, if the dynamic process has a much higher shear rate, the chain will not be able to relax into its minimum energy state during the shear process and thus eventually break differently. The experiment described in the subsequent section confirms that the quasi-static assumption is valid if $\gamma \leqslant 100\ s^{-1}$. We note that most MR applications have a shear rate within this range.

4. Experiment to determine the weak points

The above theoretical result has also been verified by experiments. Since the physics here is the same for both ER fluids and MR fluids, the experiment depicted in figure 9 is carried out with an ER fluid. There is no difficulty in carrying out a similar experiment for MR fluids.

The particles used in this experiment are glass beads coated with two layers: a metallic layer and an insulating TiO_2 surface layer. The particle diameter is about 40 μm and silicon oil is the base liquid. An electric field close to 1 kV mm^{-1} is applied across the two electrodes. The gap between the electrodes is about 2.8 mm. Therefore, there are about 70 particles in a single chain. Figure 9(a) shows that the chain shears slowly. Figure 9(b) shows that the chain breaks between the first particle and the second particle when the shear strain exceeds a critical value. This experiment repeats many times at low shear rate and we always find that the chain breaks at one end, never at the middle. Therefore, it confirms the theoretical result that the weak points of an MR or ER chain are at the chain's ends. In the experiment, we also increase the shear rate and find that the chain breaks at just one end, even at the shear rate of 200 s^{-1}.

This experiment also finds that the critical shear strain is 0.25, slightly bigger than the theoretical value 0.195. This difference may be due to the fact that the slanted chain in the experiment is usually curved, while the theoretical calculation assumes that the slanted chain is not curved.

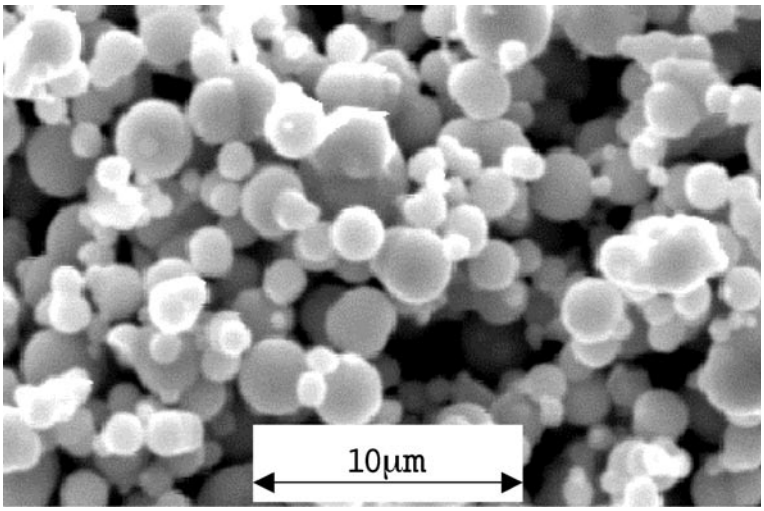

Figure 10. The SEM image of carbonyl iron particles.

While the above discussion is limited to the single-chain structure, the asymmetric breaking behaviour should be general. For example, under a magnetic field, MR chains may slowly aggregate into thick columns, whose ideal structure is a bct lattice. Such columns developed from unassisted aggregation are, in fact, a bundle of a dozen chains. Therefore, under a strong shear force, this bundle of a dozen chains may well break at one of its ends.

5. Super-strong MR fluids

After understanding the microstructure of MR fluids and identifying its weak points, we are in a position to seek a new agile approach to producing super-strong MR fluids. Let us emphasize that the strength of MR fluids comes solely from the induced microstructure. Different microstructures deliver different strengths. For example, both theoretical calculation [13] and experiment [16] have already found that a bct lattice structure has a higher yield shear stress than a single-chain structure. Unfortunately, the unassisted-aggregation process, as discussed before, is slow, produces columns of a limited thickness, and is thus not very useful. We need a technology that can rapidly produce thick columns with strong and robust ends, i.e. thick columns with no weak points at their ends.

This technology is a compression-assisted-aggregation process [17]. Immediately after a magnetic field is applied, we compress the MR fluid along the field direction before a shear force is applied. The magnetic field produces chains in milliseconds. The compression pushes these chains to form thick columns with strong and robust ends. In addition, each column consists of at least a couple of hundred chains. Once the weak points of MR microstructure are strengthened and the columns are very thick, the MR fluids become super-strong.

In our experiment, we used a suspension of carbonyl iron particles in silicone oil. The initial experiment had an MR fluid of 45% volume fraction for the purpose of making a phase-changeable flexible fixture. We later conducted experiments with low volume fractions and found that this new technology also works well at low volume fractions.

From the scanning electron micrograph (SEM) image, the carbonyl iron particles were spherical with average diameter 4.5 μm (figure 10). A small amount of surfactant, oleic acid

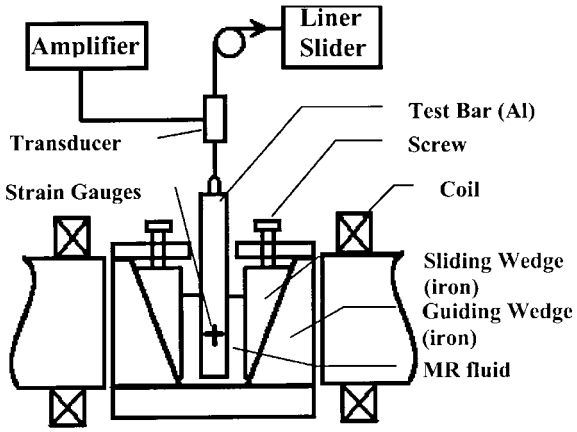

Figure 11. The experimental setup.

(Sigma), was added to the suspension so that the particles were suspended in silicon oil without settling for at least 24 h. The zero-field viscosity of our MR fluid at 45% volume fraction was 10 P.

The experimental setup is in figure 11, which was originally designed to test the idea of applying MR fluids in manufacturing flexible fixtures. An electromagnet with two water-cooled coils produced a magnetic field in the horizontal direction. The aluminium container between the two magnet poles had one sliding iron wedge and one fixed guiding iron wedge at each side. The interface between the sliding wedge and the guiding wedge had a 12° angle to the vertical direction. As the sliding wedges were pushed down, the MR fluid was compressed in the field direction. The container had a height of 115 mm and a square horizontal cross section, 89 mm $\times$ 89 mm, providing a volume of 200 ml. We poured 120 ml MR fluid into the container. Before application of the magnetic field, we inserted an aluminium bar vertically into the container centre. Then, immediately after a magnetic field was applied to solidify the MR fluid, we compressed the MR fluid by pushing the two sliding wedges down symmetrically. As the sliding wedges moved down, the MR fluid's level rose and the gap between the two poles was reduced. This inserted aluminium bar simulated a work-piece to be machined.

In order to measure the compression pressure inside the MR fluid, we used four strain gauges (FLA-5-11, Tokyo Sokki Kenkyujo Co. Ltd) on the surfaces of the test bar to form a typical Wheatstone bridge circuit, which enabled us to determine the equivalent *in situ* normal stress P_e. To determine the yield stress, we attached a force transducer (Model 3185–500) and a strain gauge conditioner–amplifier (Model 3170, Daytronic Co.) to pull the test bar out. The MR fluid is extremely strong now. We had to use a screw-driven linear slider to generate sufficient force to extract the test bar. The yield shear stress depends on the applied magnetic field and the compression pressure. Many times the MR fluid was so strong that we could lift the 170 kg magnet up through the test bar, but failed to pull the bar out from the MR fluid.

To decide the modulus, we also needed the test bar's vertical displacement under a force. The displacement was very tiny before the MR fluid had yielded. We attached a small mirror to the test bar. A tiny displacement led to a small rotation of the mirror. From a laser beam deflected by the mirror, we could determine the displacement with an accuracy of 1 μm. This displacement is so small that the tensile elongation of the test bar must be subtracted to obtain a correct shear strain.

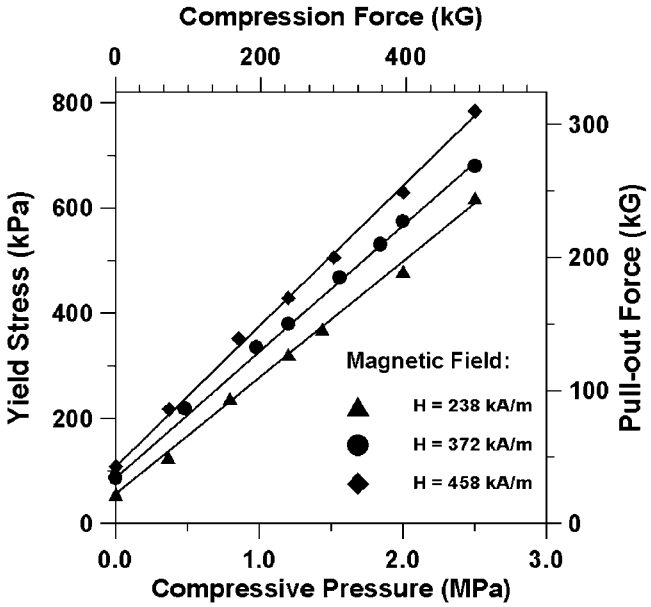

Figure 12. The yield shear stress versus the compression pressure at a different magnetic field. The yield shear stress of the MR fluid is linearly increased with the normal stress on it.

The test bar's cross section is rectangular. We denote the side perpendicular to the field as w and the side parallel to the field as t. The depth of the bar submerged in the MR fluid is h. The bottom area is $A_b = wt$. The areas perpendicular to the field or parallel to the field submerged in the MR fluid are $A_\perp = 2wh$ and $A_\parallel = 2th$, respectively. The vertical force required to pull the test bar out is mainly determined by the force due to the MR fluid, $F_{\rm MR}$. The other forces, such as the bar's weight reduced by the fluid's buoyancy, are negligibly small in comparison with $F_{\rm MR}$. We have

$$F_{\rm MR} = \tau_\perp A_\perp + \tau_\parallel A_\parallel \tag{34}$$

where $\tau_\perp$ and $\tau_\parallel$ are the yield stress on a plane perpendicular to the field direction or on a plane parallel to the field direction, respectively. By varying the size of $A_\perp$ and $A_\parallel$, we determined $\tau_\perp$ and $\tau_\parallel$. In our experiment, the four aluminium bars used had $t = 1.27$ cm and $w = 2.54$, 1.27, 0.635 and 0.3175 cm, respectively. The leading term in $F_{\rm MR}$ is $\tau_\perp A_\perp$.

Since the test bar is non-magnetic, the field around the bar is not uniform. The field H_1 at the front centre of the test bar was less than the field H_2 at the side parallel to the field. This was because some magnetic flux, instead of penetrating through the aluminium bar, bypassed it. As it was difficult to measure the field inside the solidified MR fluid and the tangential component of the magnetic field was continuous at any interface that had no surface current, we measured H_1 and H_2 at the MR fluid surface. For simplicity, we then take the average $H = (H_2 + H_1)/2$ as the mean value of H in our calculation.

Figure 12 shows $F_{\rm MR}$ versus the compression pressure for a test bar with $t = 1.27$ cm and $w = 2.54$ cm. It is clear that $F_{\rm MR}$ increases linearly with compression pressure. Hence, the yield shear stress $\tau_y(H)$ increases with the normal stress P_e. Through each measurement of $F_{\rm MR}$, the normal stress P_e and the magnetic field remain fixed. An empirical expression is given by

$$\tau_y(H) = \tau_0 + K_H P_e \tag{35}$$

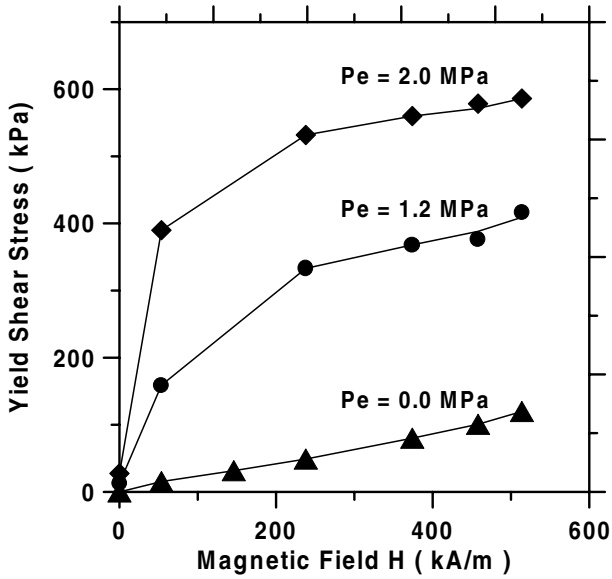

Figure 13. The yield shear stress versus the magnetic field with and without compression. All compression-assisted-aggregation processes were performed at a magnetic field of 372 kA m^{-1} first. The magnetic field was varied afterwards.

where τ_0 is the yield stress of the MR fluid without the compression-assisted aggregation. The slope K_H increases with the field H, from 0.221 for $H = 238$ kA m^{-1}, 0.239 for $H = 372$ kA m^{-1}, to 0.267 for $H = 458$ kA m^{-1}. As shown in figure 12, this linear relationship in equation (34) holds very well. In our experiment, we have obtained a static yield shear stress exceeding 800 kPa.

Figure 13 shows the effect of magnetic field on the yield stress. The MR fluid without compression-assisted aggregation has a static yield shear stress around 80 kPa at $H = 372$ kA m^{-1} and 120 kPa at $H = 514$ kA m^{-1}. The other two curves of compressed MR fluid were obtained as follows. We first applied a magnetic field of 372 kA m^{-1}, then compressed the MR fluid with a normal stress of 1.2 or 2.0 MPa, respectively. Afterwards, we varied the coil current to change the magnetic field and measured the pullout force at various fields. During the experiment, we always gave at least 30 s for the MR fluid to relax after the compression or change of magnetic field. Figure 13 clearly indicates that the yield shear stress is greatly enhanced by the compression.

We note that reducing the magnetic field below 50 kA m^{-1} after compression led to a sharp drop of the yield shear stress (figure 13). This critical magnetic field can be understood as follows. When we compressed our MR fluid, the top surface was open. Therefore, the top surface of the MR fluid has a pressure equal to atmospheric pressure. The internal pressure inside the MR fluid is not uniform under the compression. This requires that the MR microstructure be strong enough to hold the internal pressure difference. When the magnetic field is below 50 kA m^{-1}, the MR microstructure cannot hold the internal pressure difference. During the experiment, we monitored the pressure at the test bar's middle point. The built-up pressure developed by the compression also reduced at the low field, following the sharp drop of the yield stress.

When the magnetic field was off, the MR fluid had a residual yield stress of about 20 kPa and a residual field less than 0.5 kA m^{-1}. This hysteresis indicates that the magnetic particles

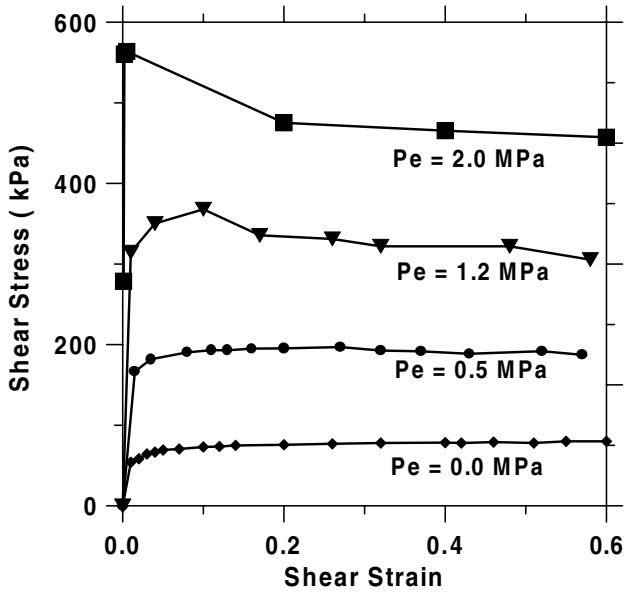

Figure 14. Shear stress versus shear strain curves with and without compression. The magnetic field for all curves is 372 kA m^{-1}.

formed a solid structure under compression-assisted aggregation and the solid structure remained after the external field was removed. However, this hysteresis was so weak that a light stir returned the MR fluid back to its liquid state immediately.

Figure 14 shows the relationship between the shear stress and shear strain. The magnetic field was 372 kA m^{-1} for all cases. Without the compression-assisted aggregation, the MR fluid began to yield at a shear stress of 40 kPa. The elastic modulus was about 10^7 Pa. After the yield point, the shear stress increases gradually until it reaches a maximum of 80 kPa at a shear strain of 0.35. With compression-assisted aggregation, the MR fluid became much stronger and more rigid. The elastic limit, the modulus and the yield shear stress were all increased dramatically. At $P_e = 2.0$ MPa, the shear modulus is as high as 5.0×10^8 Pa, 2% of aluminium's shear modulus. The overshoot of shear stress occurred at high compression pressure, indicating that the yielding process is sensitive to a structure change. A large shear strain breaks some microstructure of MR fluids and leads to a decrease of shear stress.

It is also worthwhile mentioning that the super-strong MR fluid was very stable. The shear modulus did not change in 24 h after compression-assisted aggregation, as long as the magnetic field was held. The MR fluid could be re-used many times.

6. The microstructure of super-strong MR fluids

To understand the physical mechanisms underlining this yield shear stress enhancement, we examined the microstructure of the MR fluid before and after compression-assisted aggregation. To do so, instead of silicon oil, we used polymer resins (epoxy) to mix with the iron particles at 45% volume fraction. Then, we applied a magnetic field of 372 kA m^{-1} to the new irreversible MR fluid. The resin had a cure time of one hour. In one process, we did not compress the fluid and let the resin solidify. In another process, we compressed the MR fluid with a pressure of 1.2 MPa and let the resin solidify under pressure. Afterwards, we cut the cured solid pieces

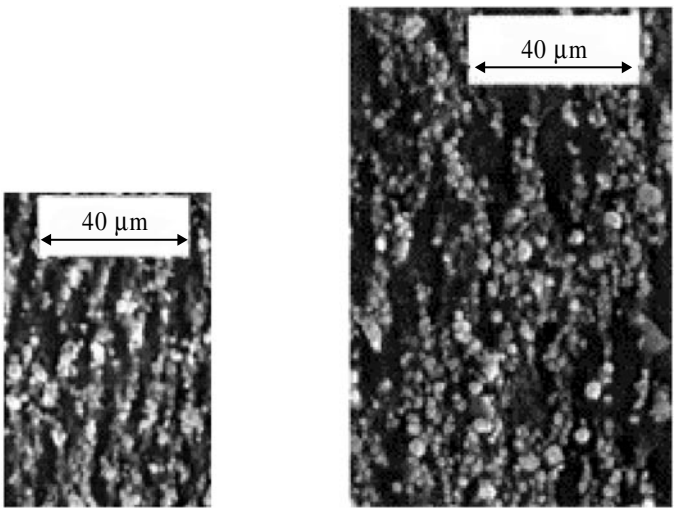

Figure 15. SEM images of iron–epoxy mixtures cured under a magnetic field of 372 kA m^{-1}. The field direction is upwards in the diagrams. (a) Without compression-assisted aggregation, the structure mainly consists of single chains. (b) The compression of 1.2 MPa forces single chains into a thick column.

with a diamond saw and conducted SEM analysis. Figure 15(a) shows the microstructure of the MR fluid without the compression. Figure 15(b) is the microstructure of the MR fluid after compression-assisted aggregation. It is clear that, without the compression, the MR fluid microstructure was dominated by single chains. As our particles were not uniform, chains were not perfect either, but all of them were not very thick, about 8 μm. As shown in figure 15(b), the MR fluid microstructure changed into thick columns after the compression. The average column thickness was over 60 μm, implying that one column had at least 120 chains in its cross section. We paid special attention to the two ends of these thick columns. As shown in the SEM picture (figure 16), the ends of these columns were much thicker than their middle. Such structures were robust and strong because the original weak points in the structure were greatly reinforced.

Our compression-assisted-aggregation process can be illustrated in figure 17. When a magnetic field is applied, magnetic particles quickly form chains. As we compress the MR fluid, chains get shorter and bent. When the chains are bent, the attraction between the chains becomes stronger and pulls these chains quickly together [11]. Meanwhile, as many particles are pushed by the plates, the ends of the columns are much thicker than their middle. These are the desirable robust structures. The columns produced by our compression process are much thicker than the product of natural aggregation.

The robust microstructure structure is the key to the super-strong MR fluids. In another experiment, we change the process order: compress the MR fluid before application of the magnetic field. Such a process does not produce any yield stress enhancement. The reason is easy to understand. Before application of the magnetic field, the magnetic particles can move freely within the base liquid. Compression before the formation of a solid structure does not create thick columns. Therefore, there is no change of yield stress.

In addition, we also note that there is a minimum strength of the magnetic chains required for successful compression. For example, if we apply the compression process when the

Figure 16. The column end of the super-strong MR fluid is much thicker than its middle.

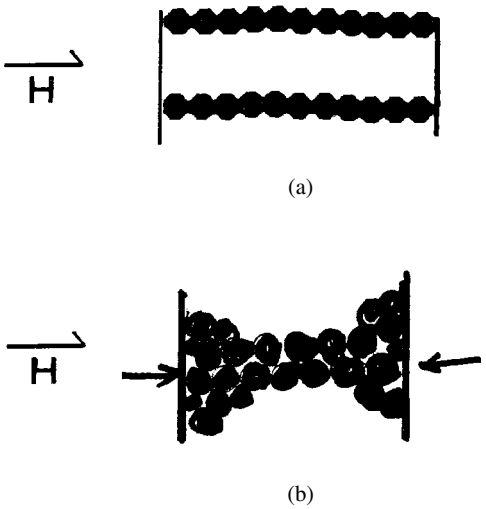

Figure 17. Formation of the robust MR microstructure during compression-assisted aggregation. (a) Chains before the compression. (b) The compression forces the chains to aggregate into thick columns with robust ends.

applied magnetic field is below 50 kA m^{-1}, then the robust thick columns cannot be produced because the original chains are too weak to sustain the pressure. Under such a situation, the original chains break and the fluid returns to a liquid state.

7. Phenomenological formula

We would like to develop a phenomenological formula here. Let us assume that the MR fluid is uniform everywhere and its stress tensor is given by $\tau_{ij}(i, j = 1, 2, 3)$, i.e. a combination of the mechanical tensor and Maxwell tensor [18]. The normal stress σ_n and shear stress τ_n on the plane with a normal direction $\vec{n}$ are given as follows:

$$\begin{aligned} \sigma_n &= \sum_{ij} \tau_{ij} n_i n_j \\ \sigma_n^2 + \tau_n^2 &= \sum_{ijl} \tau_{ij} \tau_{il} n_j n_l. \end{aligned} \tag{36}$$

If τ_{ij} has three eigenvalues $\sigma_1 \geqslant \sigma_2 \geqslant \sigma_3$ and the three principal axes are still denoted by $\vec{n}_i (i = 1, 2, 3)$, then equation (36) can be written as

$$\begin{aligned} \sigma_n &= \sigma_1 n_1^2 + \sigma_2 n_2^2 + \sigma_3 n_3^2 \\ \sigma_n^2 + \tau_n^2 &= \sigma_1^2 n_1^2 + \sigma_2^2 n_2^2 + \sigma_3^2 n_3^2. \end{aligned} \tag{37}$$

If we use the points $(\sigma_2 + \sigma_3)/2$, $(\sigma_1 + \sigma_3)/2$, $(\sigma_1 + \sigma_2)/2$ as the centres and $(\sigma_2 - \sigma_3)/2$, $(\sigma_1 - \sigma_3)/2$, $(\sigma_1 - \sigma_2)/2$ as the radii to draw Mohr circles (figure 18), the area confined by the large and two small circles defines all possible values of σ_n and τ_n [19]. As mentioned before, τ_0 is the yield stress without compression, represented by ON. The maximum allowed value of τ_n is represented by a point M, where the line NM is tangential to the biggest circle. Hence, the maximum shear stress τ_y is approximately expressed by

$$\tau_y = \tau_0 + \sigma_n \tan \phi. \tag{38}$$

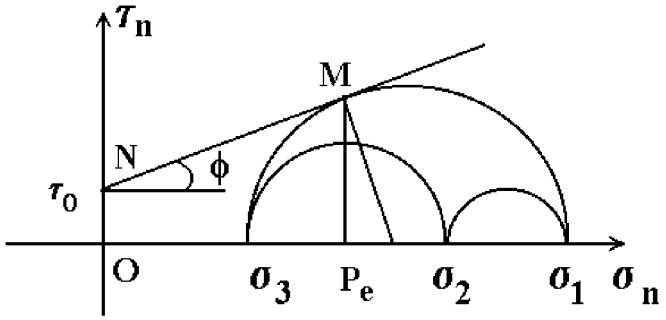

Figure 18. Mohr circle diagram to find the limiting stress. ON represents τ_0 and NM is tangential to the biggest circle.

This is the Mohr–Coulomb formula [19]. We note that this phenomenological formula is consistent with our empirical formula equation (35). Also from Coulomb's argument, $\tan\phi$ is the 'internal friction' coefficient and ϕ is the angle of 'internal friction'. If we note that P_e in equation (35) is just σ_n here, then, for example, $\tan\phi = K_H = 0.239$ or $\phi = 13.4^\circ$ at $H = 372$ kA m^{-1}. However, as mentioned before, K_H increases with magnetic field. Then the 'internal friction' increases with magnetic field. Therefore, this 'internal friction' is, in fact, mainly the magnetic force.

8. Discussions

It is well known that, in soil rheology, the soil's viscosity increases if the soil is experiencing a strong normal pressure. A similar phenomenological formula describes the soil rheology, $\tau_y = P_n \tan\phi$, where $\tan\phi$ is the friction coefficient and ϕ is about 30°–50°. In soil rheology, roughly, when P_n is greater than 0.5 MPa, the value of ϕ decreases approximately by 1° for an increment of 0.5 MPa. This is attributed to the crushed grains as the pressure increases. In our MR experiment, K_H increases with the field, while it does not appear to be reduced with the increase of P_e. This implies that the surface friction among the MR particles is small, and the field-induced interaction is the main contribution to K_H.

However, the key difference between soil rheology and our MR experiment is as follows. In soil rheology, there is a critical dilatancy occurring at volume fraction 50% for spherical particles. Only above the critical volume fraction does the soil become highly dilatant and its effective viscosity soars and supports large compressive stress under pressure, while below the critical volume fraction, the soil suspensions flow relatively easily and behave as nearly linear Newtonian [19, 20]. In our MR experiment, we see the soaring yield stress well below 50%. For example, at 25% we already see the yield stress is soaring under compression. Therefore, the key mechanism of our super-strong MR and ER fluids cannot be the dilatancy, as in soil rheology.

The test bar in our experiment is made of non-magnetic material (aluminium alloy); the 'wall effect' may underestimate the yield stress of the MR fluid [21]. However, the average MR particle size (4.5 μm) (figure 10) is much smaller than the bar's surface roughness ($\sim$30 μm). There is no reason to believe that the MR particles could slip on the surface. To verify it, we performed an experiment with several test bars with different rough surfaces. As expected, there was almost no change in the results of yield shear stress.

From the rising fluid level and the moving wedge down position, we noted that our fluid had small compressibility. This was because there were some air bubbles inside the MR fluid. The maximum compressibility ratio of the fluid was 1.5% when the fluid was compressed at $H = 372$ kA m^{-1} and pressure 2.0 MPa. Afterwards, we used a vacuum pump to extract air bubbles from the MR fluids before the experiment. This made the experiment repeatable.

To conclude this paper, we expect that super-strong MR fluids will have many industrial applications. For example, the strength of our super-strong MR fluids exceeds the requirement for manufacturing flexible fixtures and automobile clutches. Since our MR experiment was originally designed for flexible fixtures, the compression speed was not an issue here. There is no difficulties in designing an agile compression-assisted-aggregation process here. The technique described in this paper should be general and applicable to all MR fluids. In fact, the carbonyl iron-oil MR fluid used in our experiment was an old one, discovered 50 years ago [4]. There are several advanced MR fluids on the market. This technique will produce much better results with these advanced MR fluids. We also expect that the current approach is applicable to ER fluids. If the structure-enhanced yield stress of ER fluids can also be 10 times higher than the yield stress without compression-assisted-aggregation, this method will enable ER fluids to have a yield stress strong enough for many industrial applications.

Acknowledgment

This research is supported in part by a grant from NSF DMR-0075780.

References

[1] For example, see Tao R (ed) 2000 *Electrorheological Fluids and Magneto-Rheological Suspensions* (Singapore: World Scientific)
Nakano M and Koyama K (ed) 1998 *Electro-Rheological Fluids, Magneto-Rheological Suspensions and Their Applications* (Singapore: World Scientific)
[2] Hartsock D I, Novak R F and Chaundy G J 1991 *J. Rheol.* **35** 1305
[3] Carlson J D and Chrzan M J 1994 *US Patent* 5277282
Carlson J D, Chrzan M J and James F O 1994 *US Patent* 5284330
Ashour O, Rogers C A and Kordonsky W 1996 *J. Intell. Mat. Syst. Struct.* **7** 123
[4] Rabinow J 1951 *US Patent* 2575360
Rabinow J 1948 *J. AIEE Trans.* **67** 1308
[5] Winslow W M 1947 *US Patent* No 2417850
Winslow W M 1949 *J. Appl. Phys.* **20** 1137
[6] Kordonsky W I and Jacobs S D 1996 *Int. J. Mod. Phys.* B **10** 2837
[7] Ginder J M and Davis L C 1994 *Appl. Phys. Lett.* **65** 3410
[8] Tao R and Sun J M 1991 *Phys. Rev. Lett.* **67** 398
[9] Chen T J, Zitter R N and Tao R 1992 *Phys. Rev. Lett.* **68** 2555
[10] Zhou L, Wen W and Sheng P 1998 *Phys. Rev. Lett.* **81** 1509
[11] Tao R and Jiang Q 1994 *Phys. Rev. Lett.* **73** 205
[12] Halsey T C and Martin J E 1993 *Sci. Am.* **10** 58
[13] Gulley G L and Tao R 1993 *Phys. Rev.* E **48** 2744
[14] Tao R *et al* 2001 *Int. J. Mod. Phys.* B **15** 918
[15] Fu L, Macedo P B and Resca L 1992 *Phys. Rev.* B **47** 13 818
[16] Tang X, Chen Y and Conrad H 1996 *J. Intell. Mat. Syst. Struct.* **7** 517
[17] Tang X, Zhang X and Tao R 2000 *J. Appl. Phys.* **87** 2634
[18] Rosensweig R E 1995 *J. Rheol.* **39** 179
[19] For example, see Vyalov S S 1986 *Rheological Fundamentals of Soil Mechanics* (New York: Elsevier) pp 100–7
Vyalov S S 1986 *Rheological Fundamentals of Soil Mechanics* (New York: Elsevier) pp 421–40
Tuma J J and Abdel-Hady M 1973 *Engineering Soil Mechanics* (Englewood Cliffs, NJ: Prentice-Hall) pp 207–9
[20] Shook C A and Roco M C 1991 *Slurry Flow* (Woburn, MA: Butterworth-Heinemann)
[21] Lemaire E and Bossis G 1991 *J. Phys. D: Appl. Phys.* **24** 1473
Miyamoto T and Ota M 1994 *Appl. Phys. Lett.* **64** 1165